

cis-regulatory elements (4, 5). It has been proposed that this change is partially a consequence of relaxed selection pressure acting on newly evolving splice isoforms, whereas the simultaneous expression of ancestral splice isoforms allows maintenance of core gene functions (20). However, the results of this study provide evidence that rapid change in AS can also be driven by splicing changes in trans-acting regulators. The mammalian-specific skipping of PTBP1 exon 9 (or exon 8), characterized here, simultaneously affects the levels of many additional AS events. Given that the affected target exons are concentrated in genes associated with cytoskeletal and neurobiological functions and that their regulatory kinetics are significantly affected by exon 8 inclusion levels during neuronal differentiation, this event may have evolved to modulate the timing of transitions in the production of neural progenitors and mature neurons so as to affect brain morphology and complexity. Thus, a single AS event has served to amplify the rate of evolutionary change in developmentally associated AS patterns.

REFERENCES AND NOTES

1. S. B. Carroll, *Cell* **134**, 25–36 (2008).
2. C. P. Ponting, *Nat. Rev. Genet.* **9**, 689–698 (2008).
3. A. Necseulea, H. Kaessmann, *Nat. Rev. Genet.* **15**, 734–748 (2014).
4. N. L. Barbosa-Morais et al., *Science* **338**, 1587–1593 (2012).
5. J. Merkin, C. Russell, P. Chen, C. B. Burge, *Science* **338**, 1593–1599 (2012).
6. A. Reyes et al., *Proc. Natl. Acad. Sci. U.S.A.* **110**, 15377–15382 (2013).
7. P. Kafasla et al., *Biochem. Soc. Trans.* **40**, 815–820 (2012).
8. P. L. Boutz et al., *Genes Dev.* **21**, 1636–1652 (2007).
9. M. Irimia et al., *Cell* **159**, 1511–1523 (2014).
10. U. Braunschweig et al., *Genome Res.* **24**, 1774–1786 (2014).
11. Y. I. Li, L. Sanchez-Pulido, W. Haerty, C. P. Ponting, *Genome Res.* **25**, 1–13 (2015).
12. F. Robinson, C. W. Smith, *J. Biol. Chem.* **281**, 800–806 (2006).
13. E. V. Makeyev, J. Zhang, M. A. Carrasco, T. Maniatis, *Mol. Cell* **27**, 435–448 (2007).
14. Y. Xue et al., *Cell* **152**, 82–96 (2013).
15. J. A. Calarco et al., *Cell* **138**, 898–910 (2009).
16. B. Raj et al., *Mol. Cell* **56**, 90–103 (2014).
17. D. Ray et al., *Nature* **499**, 172–177 (2013).
18. M. Llorian et al., *Nat. Struct. Mol. Biol.* **17**, 1114–1123 (2010).
19. A. Han et al., *PLOS Comput. Biol.* **10**, e1003442 (2014).
20. Y. Xing, C. Lee, *Nat. Rev. Genet.* **7**, 499–509 (2006).

ACKNOWLEDGMENTS

We thank A. Dziembowski for providing DT40-Cre1 cells, U. Braunschweig for assistance with CLIP-seq analyses, and N. Barbosa-Morais and T. Sterne-Weiler for advice on statistical testing. We also acknowledge D. Torti, D. Leung, and G. O'Hanlon in the Donnelly Sequencing Centre for generating RNA-seq data. S.G. is supported by a Natural Sciences and Engineering Research Council of Canada Alexander Graham Bell Studentship, T.G.-P. is supported by fellowships from European Molecular Biology Organization and Ontario Institute for Regenerative Medicine, and M.I. was supported by a Long-Term Fellowship from the Human Frontier Science Program. This research was supported by grants from the Canadian Institutes of Health Research to B.J.B. and A.-C.G. and by a Natural Sciences and Engineering Research Council of Canada John C. Polanyi Award to B.J.B. B.J.B. holds the Banbury Chair in Medical Research at the University of Toronto. Data presented in this manuscript are archived in the Gene Expression Omnibus under accession number GSE69656.

SUPPLEMENTARY MATERIALS

www.sciencemag.org/content/349/6250/868/suppl/DC1
Materials and Methods
Figs. S1 to S12
Tables S1 and S2
References (21–25)

4 February 2015; accepted 27 July 2015
10.1126/science.aaa8381

SIGNAL TRANSDUCTION

Membrane potential modulates plasma membrane phospholipid dynamics and K-Ras signaling

Yong Zhou,¹ Ching-On Wong,¹ Kwang-jin Cho,¹ Dharini van der Hoeven,² Hong Liang,¹ Dhananiy P. Thakur,¹ Jialie Luo,¹ Milos Babic,³ Konrad E. Zinsmaier,³ Michael X. Zhu,^{1,4} Hongzhen Hu,^{1,4} Kartik Venkatachalam,^{1,4} John F. Hancock^{1,4*}

Plasma membrane depolarization can trigger cell proliferation, but how membrane potential influences mitogenic signaling is uncertain. Here, we show that plasma membrane depolarization induces nanoscale reorganization of phosphatidylserine and phosphatidylinositol 4,5-bisphosphate but not other anionic phospholipids. K-Ras, which is targeted to the plasma membrane by electrostatic interactions with phosphatidylserine, in turn undergoes enhanced nanoclustering. Depolarization-induced changes in phosphatidylserine and K-Ras plasma membrane organization occur in fibroblasts, excitable neuroblastoma cells, and *Drosophila* neurons in vivo and robustly amplify K-Ras-dependent mitogen-activated protein kinase (MAPK) signaling. Conversely, plasma membrane repolarization disrupts K-Ras nanoclustering and inhibits MAPK signaling. By responding to voltage-induced changes in phosphatidylserine spatiotemporal dynamics, K-Ras nanoclusters set up the plasma membrane as a biological field-effect transistor, allowing membrane potential to control the gain in mitogenic signaling circuits.

Plasma membrane (PM) potential (V_m) has been linked to cell survival and proliferation (1, 2). Dividing cells are more depolarized than quiescent cells, and oncogenically transformed cells are generally more depolarized than normal parental cells, indicating that V_m may be inversely coupled to pro-proliferative pathways (2). The mechanisms that might link V_m to cell proliferation are poorly characterized. Ras proteins are membrane-bound signaling proteins involved in cell differentiation, proliferation, and survival (3). The three ubiquitously expressed Ras isoforms—H-, N-, and K-Ras—assemble into spatially distinct nanoassemblies on the PM called nanoclusters (4). Nanocluster formation is essential for activation of mitogen-activated protein kinase (MAPK) signaling by Ras because activation of the protein kinase RAF on the PM is restricted to Ras.GTP (GTP, guanosine triphosphate) nanoclusters (5). Nanocluster assembly requires complex interactions between PM lipids and the Ras lipid anchors, C-terminal hyper-variable regions, and G domains; with interactions between Ras basic residues and charged PM lipids being particularly relevant (6). The diffusion of lipids in model membranes and phase separation of multicomponent bilayers

is responsive to electric fields (7, 8). We therefore tested whether the lateral distribution of anionic lipids in the PM is responsive to V_m and the potential consequences on Ras spatial organization.

We manipulated the V_m of baby hamster kidney (BHK) cells, measured by whole-cell patch clamping, by changing extracellular K^+ concentration (Fig. 1A). Simultaneously we quantified the nanoscale distribution of various green fluorescent protein (GFP)-labeled lipid-binding probes on the inner PM by using electron microscopy (EM) and spatial mapping (4, 9, 10). The analyses show that nanoclustering of phosphatidylserine (PS) and phosphatidylinositol 4,5-bisphosphate (PIP₂) was enhanced on PM depolarization, whereas there was no detectable change in the lateral distribution of phosphatidic acid (PA) or phosphatidylinositol 3,4,5-trisphosphate (PIP₃) (Fig. 1, B and C, and fig. S1). The enhanced clustering of PS was fast, being 80% complete within 30 s (the shortest assay time allowed by the EM technique) (Fig. 1D). PIP₂ clustering increased at a slightly slower rate (Fig. 1D). On repolarization of the PM, by switching from 100 mM $[K^+]$ back to 5 mM $[K^+]$, nanoclustering of PS and PIP₂ reverted to control values with near identical kinetics (Fig. 1E). The PS content of the PM was unaffected by changing V_m (fig. S2). Fluorescence recovery after photobleaching assays of lipid spatiotemporal dynamics showed that the mobile fraction of fluorescently labeled PS and PIP₂ decreased significantly upon PM depolarization (fig. S3), consistent with the EM data. The differential effect of V_m on anionic PM lipids is concordant with observations that charged lipids respond differently to applied electric fields (7, 8, 11).

¹Department of Integrative Biology and Pharmacology, Medical School, University of Texas Health Science Center at Houston, Houston, TX 77030, USA. ²Department of Diagnostic and Biomedical Sciences, Dental School, University of Texas Health Science Center at Houston, Houston, TX 77054, USA. ³Department of Neuroscience, University of Arizona, Tucson, AZ 85721, USA. ⁴Program in Cell and Regulatory Biology, University of Texas Graduate School of Biomedical Sciences, Houston, TX 77030, USA. *Corresponding author. E-mail: john.f.hancock@uth.tmc.edu

The localization and lateral distribution of K-Ras on the PM requires electrostatic interactions between a C-terminal polybasic domain and PS (9, 10, 12, 13). The electrostatic potential of the inner PM leaflet is independent of V_m , and concordantly total internal reflection fluorescence and confocal microscopy showed that K-Ras PM localization was insensitive to PM depolarization (fig. S5). However, EM spatial mapping experiments of BHK cells expressing GFP-K-RasG12V (GFP-labeled, constitutively GTP-bound K-Ras) showed that K-RasG12V peak $L(r) - r$ (L_{\max} , where L represents a K function and r is radius) values correlated strongly with V_m , indicating that PM depolarization enhances K-Ras nanoclustering (Fig. 1F). The temporal dynamics of V_m -induced changes in K-RasG12V nanoclustering matched those of PS rather than PIP₂ (Fig. 1, D and E). To visualize nanocluster changes in intact cells, we used fluorescence lifetime imaging microscopy combined with fluorescence resonance energy transfer (FLIM-FRET). The fluorescence lifetime of GFP-K-RasG12V in cells coexpressing the FRET acceptor red fluorescent protein (RFP)-K-RasG12V decreased as a function of V_m (Fig. 1, G and H), indicating increased FRET between GFP-K-

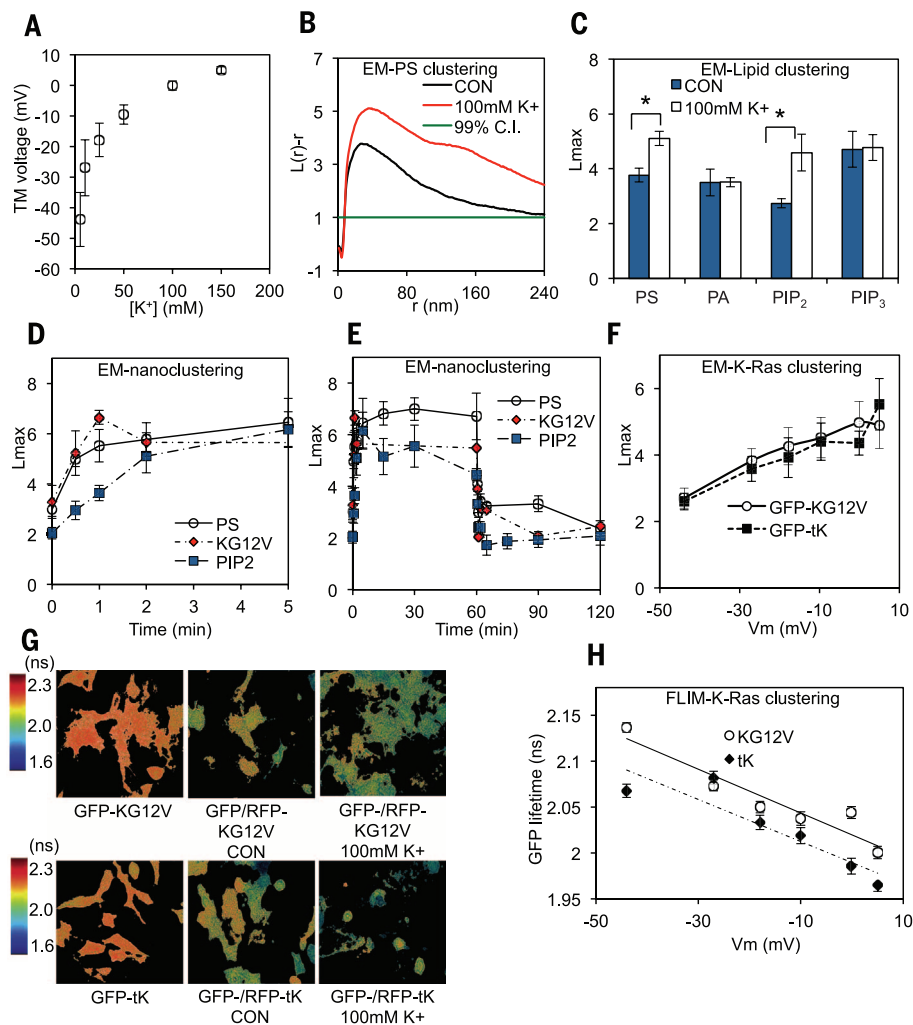
RasG12V and RFP-K-RasG12V and hence increased K-Ras nanoclustering. Conversely, expression of the Kv2.1 channel, which hyperpolarizes the PM (14) (fig. S6C), largely eliminated FRET between GFP-K-RasG12V and RFP-K-RasG12V, consistent with disruption of K-Ras nanoclustering (fig. S6). Expression of a nonconducting channel mutant, Kv2.1W369CY384T (fig. S6C), had no effect on the lifetime of GFP-K-RasG12V in control FLIM experiments (fig. S6B). PM depolarization did not change concentrations of intracellular Ca²⁺ in BHK cells (fig. S7). Concordantly, we obtained identical EM and FLIM results in Ca²⁺-free buffers containing the Ca²⁺ chelator EGTA (fig. S8). PM depolarization also enhanced the nanoclustering of GFP-tK but not GFP-tH (GFP coupled to the isolated membrane-anchoring domains of K-Ras and H-Ras, respectively) (Fig. 1, F to H, and fig. S8, D and E). Thus, K-Ras nanoclustering is sensitive to V_m through a mechanism that requires the C-terminal polybasic domain.

In excitable differentiated mouse Neuro2A (N2A) neuroblastoma cells (15), PM depolarization with high [K⁺] also caused a significant decrease in GFP fluorescence lifetime in GFP-tK

and RFP-tK coexpressing cells (Fig. 2, A and B), indicating increased GFP-RFP FRET from increased GFP-tK clustering. Similar results were observed with full-length K-RasG12V (Fig. 2, A and B). Glutamate receptor-induced PM depolarization (15) also enhanced K-RasG12V clustering (Fig. 2C). This effect appeared unrelated to activation of phospholipase C (PLC), because pretreatment with the PLC inhibitor U73122 did not abrogate glutamate-stimulated K-Ras clustering but effectively blocked increases in intracellular concentrations of Ca²⁺ (fig. S9). Thus, glutamate-induced changes in K-Ras nanoclustering are also mediated through a change in PM voltage.

We evaluated the causality between V_m -induced changes in PS or PIP₂ distribution and K-Ras clustering by quantifying their colocalization using EM spatial mapping and integrated bivariate K functions (LBI values) (9). PM depolarization significantly and selectively enhanced the association of K-Ras with PS but not with PIP₂ (Fig. 3A and fig. S10), consistent with V_m -induced changes in the PM PS distribution being causally associated with increased K-Ras nanoclustering. We therefore evaluated K-Ras clustering in PS auxotroph (PSA-3) cells (16), which, when grown

Fig. 1. PM depolarization enhances nanoclustering of lipids and K-Ras. (A) Whole-cell patch clamping of BHK cells to measure V_m in isotonic buffers containing different [K⁺]. (B) Weighted mean K functions shown as $L(r) - r$ for a PS lipid probe ($n \geq 8$) in control (CON) and depolarized BHK cells. $L(r) - r$ values >99% confidence interval (C.I.) for a random pattern indicate clustering. Depolarization (100mM [K⁺]) significantly increased PS clustering ($P < 0.001$, bootstrap test). (C) Peak $L(r) - r$ values, L_{\max} , derived from curves as in (B), quantify the extent of nanoclustering of lipid probes for PS, PIP₂, PA, or PIP₃ in control and depolarized (100 mM [K⁺]) BHK cells. (D) Short time course (<5 min) of changes in L_{\max} values for PS, PIP₂, and GFP-K-RasG12V (KG12V) in BHK cells depolarized with 100 mM [K⁺] at $t = 0$ min. (E) Time course of depolarization (5 to 100 mM [K⁺] at $t = 0$ min) and repolarization (100 to 5 mM [K⁺] at $t = 60$ min), changes in L_{\max} for PS, PIP₂, and K-RasG12V. (F) Dependence of GFP-K-RasG12V or GFP-tK clustering, quantified as L_{\max} values, on V_m varied as in (A). (G) FLIM images (GFP) of cells expressing GFP/RFP-K-RasG12V and GFP/RFP-tK FRET pairs. (H) Fluorescence lifetime of GFP-K-RasG12V or GFP-tK in cells expressing the cognate RFP-FRET pair plotted against V_m . Each point is the mean (\pm SEM) GFP lifetime measured in >60 individual cells. Significant differences (* $P < 0.001$) were evaluated by using one-way analysis of variance (ANOVA). Error bars in all panels represent SEM.



in the absence of ethanolamine, synthesize ~30% less total PS (16) and are depleted of PS in the inner PM leaflet (9, 16). EM-spatial mapping and FLIM-

FRET imaging of ethanolamine-starved PSA-3 cells showed that PS depletion rendered K-Ras nanoclustering insensitive to V_m (Fig. 3, B and C).

Enhancing K-Ras.GTP nanoclustering increases activation of the RAF-MAPK cascade (5). We therefore examined the effect of V_m on

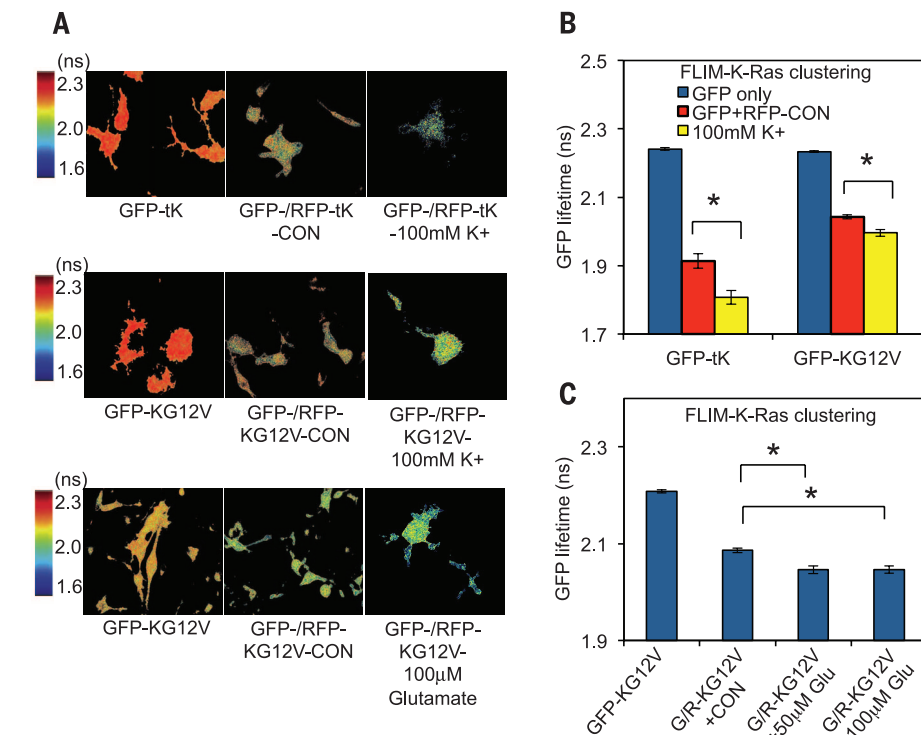


Fig. 2. Plasma membrane depolarization enhances K-Ras nanoclustering in mouse neuroblastoma cells.

(A) FLIM images of differentiated N2A cells expressing the FRET pairs: RFP/GFP-tK or RFP/GFP-K-RasG12V (GFP-KG12V) and depolarized with 100 mM $[K^+]$ or 50 to 100 μ M glutamate (Glu). (B and C) Quantification of fluorescence lifetime of GFP-K-RasG12V or GFP-tK in N2A cells expressing the cognate RFP-FRET pair treated as in (A). Each data point is the mean (\pm SEM) GFP lifetime measured in >60 individual cells. Significant differences (* $P < 0.01$) were evaluated by using one-way ANOVA.

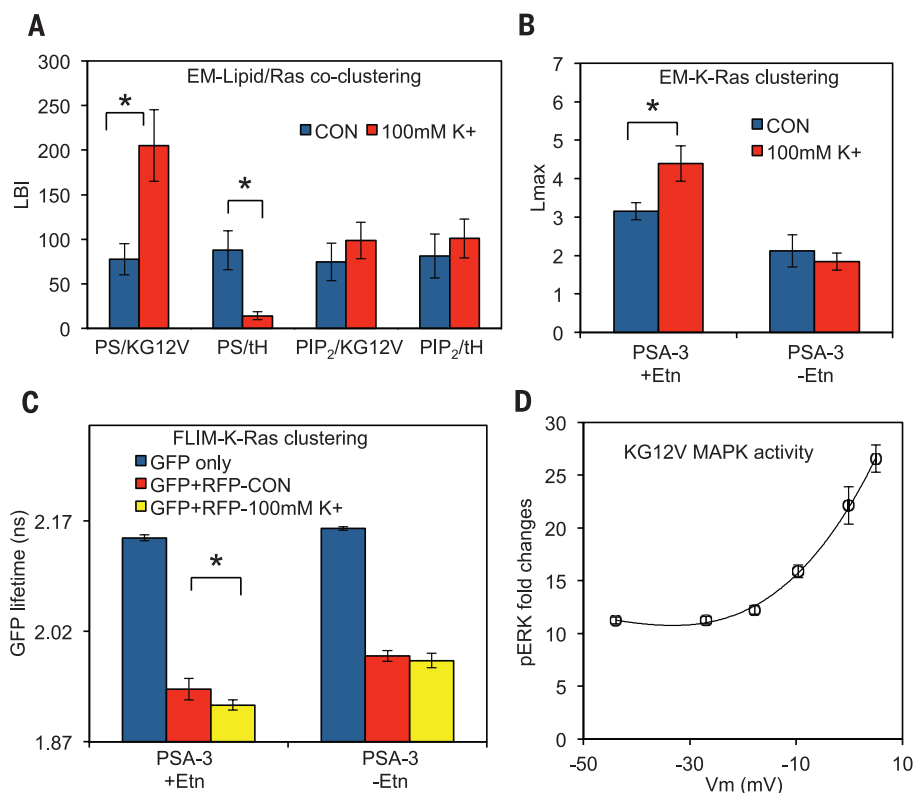
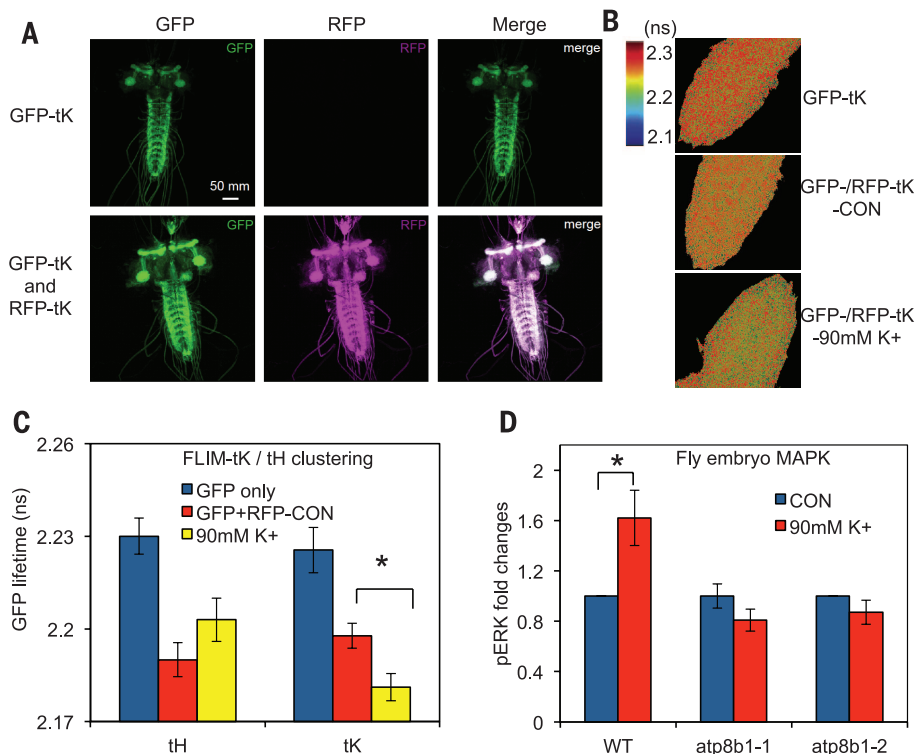


Fig. 3. PS mediates V_m -induced changes in K-Ras nanoclustering and signaling.

(A) PM sheets from BHK cells expressing RFP-K-RasG12V, and a GFP-tagged lipid-binding probe for PS or PIP₂, were labeled with anti-GFP-6nm gold and anti-RFP-2nm gold and visualized by EM. Bivariate K functions (summarized as LBI values) were used to quantify the colocalization of PS or PIP₂ with GFP-K-RasG12V and GFP-tH nanoclusters. Statistical significance was evaluated in Mann-Whitney tests (* $P < 0.05$). Additional lipid reorganization results are shown in fig. S10E. (B) Univariate EM-spatial mapping of PM sheets prepared from PSA-3 cells expressing GFP-K-RasG12V and grown with or without ethanolamine (\pm Etn). (C) FLIM imaging of PSA-3 cells expressing GFP-K-RasG12V or coexpressing RFP-K-RasG12V and grown \pm Etn. (D) MAPK activation in K-RasG12V-transformed BHK cells (and wild-type cells fig. S11) measured by quantitative immunoblotting for phosphorylated ERK (pERK) after PM depolarization as in Fig. 1A.

Fig. 4. Enhanced K-Ras clustering and MAPK signaling in intact fly embryo after PM depolarization. (A) Confocal images of flies expressing GFP-tK, or coexpressing GFP-tK and RFP-tK, from a neuronal-specific promoter. (B) FLIM imaging of brains from flies in (A) in control buffer and after depolarization with high $[K^+]$. (C) Quantification of fluorescence lifetime of GFP-tK in fly brains expressing the cognate RFP-FRET pair treated as in (B); results are mean (\pm SEM, $n = 9$). High $[K^+]$ had no effect on the fluorescence lifetime of GFP-tK in fly brains expressing GFP-tH and RFP-tH. (D) Fly embryos from wild-type (WT) and mutant *atp8b* flies incubated in 5 or 90 mM K^+ for 15 min and then immunoblotted for pERK. Results are quantified as mean \pm SEM ($n = 3$).



K-Ras-specific MAPK signaling. Progressively reducing V_m enhanced phosphorylation of extracellular signal-regulated kinase (ERK) in K-RasG12V-expressing cells (Fig. 3D and figs. S11 and S12), consistent with the EM and FLIM results. ERK activation was nonlinearly dependent on V_m (Fig. 3D) unlike L_{max} (Fig. 1F). This is expected because the K-Ras clustered fraction (ϕ), which determines MAPK signaling output (5), is a nonlinear function of L_{max} (4) (fig. S13). MAPK activation increased rapidly in response to PM depolarization (<30 s), concordant with the time scale of enhanced K-Ras clustering, and recovered within 30 min of PM repolarization (fig. S14). V_m -induced activation of MAPK signaling in K-RasG12V-expressing PSA-3 cells was abolished under conditions of PS depletion (fig. S11C). Thus, depleting cellular and PM PS levels effectively uncouples V_m from K-Ras clustering and signaling. Because the amounts of K-Ras.GTP are fixed in K-RasG12V cells, V_m regulates signal gain in the K-Ras signaling circuit by controlling the extent of K-Ras nanoclustering.

Last, we observed similar results in vivo in *Drosophila* (Fig. 4A) (17). Depolarization of intact fly brains expressing GFP-tK and RFP-tK resulted in increased GFP-RFP FRET (Fig. 4, B and C), indicating enhanced K-Ras clustering. Concordantly, depolarization of wild-type fly embryos significantly stimulated MAPK activation, whereas depolarization of *atp8b* mutant embryos (fig. S15) that lack a PM PS flippase (18, 19) had no effect on MAPK activation (Fig. 4D and fig. S16L). Lack of *atp8b* diminishes the inner PM leaflet of PS (18, 19) (fig. S16, A to K) and is thus

a partial phenocopy of PS-deficient PSA-3 cells (fig. S11).

We show that PM depolarization induces rapid and substantial changes in the nanoscale organization of the anionic phospholipids, PS and PIP₂, on the inner leaflet of the PM. An important consequence of the PS reorganization is increased K-Ras nanoclustering, which enhances K-Ras-dependent MAPK signaling in nonexcitable and excitable cells, as well as intact fly embryo. Reduced PM V_m has long been associated with cell survival, proliferation, and differentiation (1, 2). Yet, no compelling mechanism has been proposed to explain the input of electrical signal to cell signaling cascades. We suggest that K-Ras nanoclusters, by responding to V_m -induced changes in PS spatiotemporal dynamics, allow the PM to act as a field-effect transistor to control the gain in Ras signaling circuits. Neuronal development, including plasticity, long-term potentiation, and memory, is strongly associated with V_m and MAPK signaling (20, 21); it is thus feasible that changes in PS-mediated K-Ras lateral segregation potentially play an important role these processes.

REFERENCES AND NOTES

- S. Sundelacruz, M. Levin, D. L. Kaplan, *Stem Cell Rev.* **5**, 231–246 (2009).
- D. J. Blackiston, K. A. McLaughlin, M. Levin, *Cell Cycle* **8**, 3527–3536 (2009).
- J. F. Hancock, *Nat. Rev. Mol. Cell Biol.* **4**, 373–385 (2003).
- S. J. Plowman, C. Muncke, R. G. Parton, J. F. Hancock, *Proc. Natl. Acad. Sci. U.S.A.* **102**, 15500–15505 (2005).
- T. Tian *et al.*, *Nat. Cell Biol.* **9**, 905–914 (2007).

- Y. Zhou, J. F. Hancock, *Biochim. Biophys. Acta* **1853**, 841–849 (2015).
- P. S. O'Shea, S. Feuerstein-Thelen, A. Azzi, *Biochem. J.* **220**, 795–801 (1984).
- J. T. Groves, S. G. Boxer, H. M. McConnell, *Proc. Natl. Acad. Sci. U.S.A.* **95**, 935–938 (1998).
- Y. Zhou *et al.*, *Mol. Cell. Biol.* **34**, 862–876 (2014).
- N. Ariotti *et al.*, *J. Cell Biol.* **204**, 777–792 (2014).
- T. Starke-Peterkovic, R. J. Clarke, *Eur. Biophys. J.* **39**, 103–110 (2009).
- T. Yeung *et al.*, *Science* **319**, 210–213 (2008).
- K. J. Cho *et al.*, *J. Biol. Chem.* **287**, 43573–43584 (2012).
- K. S. Park, D. P. Mohapatra, H. Misonou, J. S. Trimmer, *Science* **313**, 976–979 (2006).
- J. B. Van der Valk, H. P. Vijverberg, *Eur. J. Pharmacol.* **185**, 99–102 (1990).
- S. Lee *et al.*, *Genes Cells* **17**, 728–736 (2012).
- A. H. Brand, N. Perrimon, *Development* **118**, 401–415 (1993).
- T. S. Ha, R. Xia, H. Zhang, X. Jin, D. P. Smith, *Proc. Natl. Acad. Sci. U.S.A.* **111**, 7831–7836 (2014).
- C. C. Paulusma *et al.*, *Hepatology* **47**, 268–278 (2008).
- S. Impey, K. Obrietan, D. R. Storm, *Neuron* **23**, 11–14 (1999).
- R. J. Kelleher 3rd, A. Govindarajan, H. Y. Jung, H. Kang, S. Tonegawa, *Cell* **116**, 467–479 (2004).

ACKNOWLEDGMENTS

This work was supported by grant RP130059 from the Cancer Prevention and Research Institute of Texas and grant ROINS081301 from NIH.

SUPPLEMENTARY MATERIALS

www.sciencemag.org/content/349/6250/873/suppl/DC1
Materials and Methods
Figs. S1 to S16

23 December 2014; accepted 2 July 2015
10.1126/science.aaa5619

This copy is for your personal, non-commercial use only.

If you wish to distribute this article to others, you can order high-quality copies for your colleagues, clients, or customers by [clicking here](#).

Permission to republish or repurpose articles or portions of articles can be obtained by following the guidelines [here](#).

The following resources related to this article are available online at www.sciencemag.org (this information is current as of September 10, 2015):

Updated information and services, including high-resolution figures, can be found in the online version of this article at:

<http://www.sciencemag.org/content/349/6250/873.full.html>

Supporting Online Material can be found at:

<http://www.sciencemag.org/content/suppl/2015/08/19/349.6250.873.DC1.html>

A list of selected additional articles on the Science Web sites **related to this article** can be found at:

<http://www.sciencemag.org/content/349/6250/873.full.html#related>

This article **cites 21 articles**, 10 of which can be accessed free:

<http://www.sciencemag.org/content/349/6250/873.full.html#ref-list-1>

This article has been **cited by** 1 articles hosted by HighWire Press; see:

<http://www.sciencemag.org/content/349/6250/873.full.html#related-urls>

This article appears in the following **subject collections**:

Cell Biology

http://www.sciencemag.org/cgi/collection/cell_biol



Supplementary Materials for

Membrane potential modulates plasma membrane phospholipid dynamics and K-Ras signaling

Yong Zhou, Ching-On Wong, Kwang-jin Cho, Dharini van der Hoeven, Hong Liang, Dhananiay P. Thakur, Jialie Luo, Milos Babic, Konrad E. Zinsmaier, Michael X. Zhu, Hongzhen Hu, Kartik Venkatachalam, John F. Hancock*

*Corresponding author. E-mail: john.f.hancock@uth.tmc.edu

Published 21 August 2015, *Science* **349**, 873 (2015)
DOI: 10.1126/science.aaa5619

This PDF file includes:

Materials and Methods
Figs. S1 to S16

Materials and Methods

Materials

BHK cells were maintained in DMEM (10% BCS) while CHO cells were grown in F-12K (10% FBS). Mutant PSA-3 cells were grown in F-12K with dialyzed FBS for at least 72 hours to ensure efficient PS depletion while 10 μ M ethanolamine was added to the media to recover PS level back to the wild-type level (16). Neuroblastoma (N2A) cells were cultured in DMEM containing 10% FBS and incubated in serum-free DMEM over-night to allow sufficient differentiation. Dr. Sergio Grinstein (The Hospital for Sick Children, Toronto, Canada) generously provided GFP-LactC2 (lactadherin C2 domain) as a specific probe for PS. Dr. Guangwei Du (University of Texas Health Science Center, Houston, Texas, USA) kindly provided GFP-Spo20 (PA-binding domain derived from *Saccharomyces cerevisiae* protein Spo20), GFP-PH-PLC δ (pleckstrin homology, PH, domain of phospholipase C-delta specifically for binding to PIP₂) and GFP-PH-Akt (PH domain of Akt and a PIP₃ probe) (9). HEPES buffer contains NaCl 140mM, KCl 5mM, CaCl₂ 2mM, MgCl₂ 1mM, HEPES 10mM, Glucose 10mM, sucrose 30mM. Solution pH was adjusted to 7.4 with NaOH. For high K⁺ solution, NaCl was replaced with an equal molar concentration of KCl and other components remained the same. For Ca²⁺-free buffer, MgCl₂ was adjusted to 2mM while additional 1mM EGTA was added to quench any trace amount of Ca²⁺. Fluorescent lipids, TopFluor-PS (TF-PS) or TopFluor-PIP₂ (TF-PIP₂), were purchased from Avanti Polar Lipids in powder form, dissolved in chloroform as stock (1mg/ml) and stored at -20°C under N₂.

Methods

Immuno-electron microscopy (EM) spatial mapping:

Univariate K-function: Immuno-EM was conducted as described in our previous studies (4, 5, 9). Briefly, Intact cell plasma membrane sheets of BHK cells expressing the GFP-tagged protein of interest were attached to EM grids, washed with PBS, fixed with 4% PFA and 0.1% glutaraldehyde, labeled with 4.5nm gold particles coupled to anti-GFP antibody and embedded in uranyl acetate. Gold particle distribution on the plasma membrane sheets was imaged using a JEOL JEM-1400 transmission EM at 100,000x magnification and (x,y) coordinates of each gold particle within a selected 1 μ m² area determined using ImageJ. The clustering of gold particles was analyzed using variations of Ripley's K-function (4, 5) (Eqs. 1 and 2):

$$K(r) = An^{-2} \sum_{i \neq j} w_{ij} 1(\|x_i - x_j\| \leq r) \quad (\text{Eq. 1})$$

$$L(r) - r = \sqrt{\frac{K(r)}{\pi}} - r \quad (\text{Eq. 2})$$

where $K(r)$ is the univariate K-function for n gold particles in the area A ; r is radius; $\|\cdot\|$ is Euclidean distance; $1(\cdot)$ is the indicator function that has a value of 1 if $\|x_i - x_j\| \leq r$ and 0 otherwise; and w_{ij}^{-1} is the proportion of the circumference of a circle with center at x_i and a radius $\|x_i - x_j\|$ located within A . $L(r) - r$ is standardized on the 99% confidence interval estimated from Monte Carlo simulations. A minimum of 15 plasma membrane sheets

were imaged and analyzed for each experiment. The statistical significance of differences between replicated point patterns was evaluated in bootstrap tests constructed as described (4).

Bivariate K-function: co-localization of two populations of proteins/lipids labeled by different sized gold particles was evaluated using bivariate K-functions (4, 9). PM sheets were prepared fixed and labeled with 2nm gold coupled to anti-RFP antibody and 6nm gold coupled to anti-GFP antibody. The (x,y) coordinates of each small and large gold particle within a selected $1\mu\text{m}^2$ area determined using ImageJ. Bivariate K-functions were calculated as in Eqs. 3-6:

$$K_{biv}(r) = (n_b + n_s)^{-1}[n_b K_{sb}(r) + n_s K_{bs}(r)] \quad (\text{Eq. 3})$$

$$K_{bs}(r) = \frac{A}{n_b n_s} \sum_{i=1}^{n_b} \sum_{j=1}^{n_s} w_{ij} 1(\|x_i - x_j\| \leq r) \quad (\text{Eq. 4})$$

$$K_{sb}(r) = \frac{A}{n_b n_s} \sum_{i=1}^{n_s} \sum_{j=1}^{n_b} w_{ij} 1(\|x_i - x_j\| \leq r) \quad (\text{Eq. 5})$$

$$L_{biv}(r) - r = \sqrt{\frac{K_{biv}(r)}{\pi}} - r \quad (\text{Eq. 6})$$

where $K_{bs}(r)$ describes the distribution of the 6nm (b=big) gold particles with respect to each 2nm (s=small) gold particle and reciprocally $K_{sb}(r)$ describes the distribution of small gold particles with respect to each big gold particle. The two functions are combined to generate a single $K_{biv}(r)$ estimator where n_b = number of 6-nm gold particles and n_s = number of 2-nm gold particles and other notation is as in Eq 1 and 2. $L_{biv}(r)-r$ is further standardized on the 95% confidence interval estimated from Monte Carlo simulations. LBI is a defined integral of the standardized $L_{biv}(r)-r$ function used to provide a summary statistic of extent of co-localization (24):

$$LBI = \int_8^{120} Std L_{biv}(r) - r - 1 . dr \quad (\text{Eq. 7})$$

For each experiment a minimum of 15 plasma membrane sheets were imaged and analyzed. Mann Whitney tests were used to evaluate the statistical significance of differences between LBI values.

Fluorescence lifetime imaging microscopy combined with fluorescence resonance energy transfer (FLIM-FRET):

Cells expressing GFP-tagged protein alone or co-expressing both GFP-tagged and RFP-tagged proteins were washed with PBS, fixed in 4% PFA and quenched with 50mM NH_4OH . Standardized transfection protocols were used to closely match expression of each member of the FRET pair. Cells were imaged using an x60 Plan-Apo/1.4NA oil emersion lens mounted on a wide field Nikon Eclipse microscope. GFP was sinusoidally excited by a modulating 3-Watt 497nm light-emitting diode (LED) at 40 MHz and fluorescence lifetime measured using a Lambert Instrument (Roden, the Netherlands) FLIM unit. At least 60 individual cells were imaged and lifetime (phase) values were

pooled and averaged. Each experiment was replicated 3 times. Statistical analysis was performed using one-way ANOVA. For fly FLIM experiments, 3rd instar larvae expressing the GFP/RFP constructs in the nervous system were filleted and fixed in 4% PFA prior to mounting in Vectashield and FLIM-FRET imaging. Confocal images of the fly brains were imaged on Nikon A1 confocal microscope using a 20x Air objective.

Western blots:

MAPK signaling activity was examined in wild-type BHK cells, BHK cells expressing GFP-K-RasG12V, BHK cells expressing GFP-H-RasG12V, CHO cells expressing GFP-K-RasG12V, or PSA-3 cells (in dialyzed FBS or supplemented with 10mM ethanolamine) expressing GFP-K-RasG12V. PS depletion was achieved by incubating PSA-3 cells in dialyzed FBS for at least 72h, PS levels were maintained at control levels by supplementing the growth medium of PSA-3 cells with 10 μ M ethanolamine. On the day of experiments, cells were washed with HEPES buffers containing various [K⁺], incubated in the same buffers for up to 1h and harvested. Whole cell lysates were collected as described (9) and immunoblotted for pMEK, pERK and pAkt.

Drosophila genetics and husbandry:

cDNAs encoding GFP-tH, RFP-tH, GFP-tK, RFP-tK, and LactC2-mCherry (LC2-mCherry) were subcloned vectors containing Upstream Activation Sequence (UAS). Transgenic flies carrying the UAS expression constructs were generated by attB-attP integration by injecting the constructs to fly embryos. *pUAS-GFP-tH* and *pUAS-GFP-tK* were injected to 2nd chromosome, *pUAS-RFP-tH* and *pUAS-RFP-tK* to 3rd chromosome, and *pUAS-LC2-mCherry* to 2nd chromosome. We used *elav-GAL4* to express these constructs in fly neurons. Wild-type (*w¹¹¹⁸*) and two mutant alleles of the *Drosophila* flippase homolog *atp8b* (*CG14741*) were obtained from Bloomington Stock Center. *atg8b¹* and *atg8b²* correspond to *CG14741^{f05203}* and *CG14741^{M106979}* respectively. All flies were reared in vials with standard cornmeal based food at room temperature (~22°C). The ingredients in 1 L of liquid fly food were: 95 g agar, 275 g Brewer's yeast, 520 g of cornmeal, 110 g of sugar, and 45 g of propionic acid. 36 g of Tegosept was dissolved in 92 ml of 95% ethanol and added to the mixture to prevent bacterial growth.

Western blotting of whole Drosophila embryo:

Flies were transferred to cages containing grape juice agar (Genesee Scientific) for egg-laying for 14 hours. Cages were cleared of flies for 2 hours before collecting the embryos from the surface of the agar. Embryos were dechorionated in 50% bleach for 5 minutes. After washing 3 times with PBS, embryos were bathed in either 5mM K⁺ or 90mM K⁺ HL-3 for 20 minutes, before homogenized in 2X Laemmli sample buffer (Bio-Rad). 5K⁺ HL-3 contained: 5 mM KCl, 70 mM NaCl, 20 mM MgCl₂, 10 mM NaHCO₃, 0.5 mM CaCl₂, 115 mM sucrose, 5 mM trehalose, and 5 mM HEPES (pH7.2). 90K⁺ HL-3 contained: 90 mM KCl, 40mM NaCl, 20 mM MgCl₂, 10 mM NaHCO₃, 0.5 mM CaCl₂, 115 mM sucrose, 5 mM trehalose, and 5 mM HEPES (pH7.2). Total lysate from ~7-10 embryos was loaded onto each lane of 10% Tris-glycine gel (Bio-Rad). Blots were probed with primary antibodies against pERK and α -tubulin. After overnight incubations with the primary antibodies, the blots were washed and probed with IRDye 680 donkey anti-rabbit IgG (LI-COR) and IRDye 800 donkey anti-mouse IgG (LI-COR), and signals were detected with the Odyssey infrared imaging system (LI-COR). Blot images were analyzed using ImageJ (National Institutes of Health).

Immunohistochemistry of Drosophila larvae:

Wandering third instar larvae expressing LC2-mCherry pan-neuronally (*elav-GAL4*) or in fat-bodies (*Cg-GAL4*) were pinned on Sylgard silicone elastomer (Dow Corning), and bathed in ice-cold phosphate-buffered saline (PBS). The body wall was cut open along the dorsal midline, and the gut was removed. The remaining fillet containing the nervous system and fat bodies was pinned flat and fixed with 4% paraformaldehyde in PBS for 30 minutes. The fixed larval fillets were washed with 0.1% Triton X-100 in PBS (PBST) before antibody incubation. Fillets of controls and *atp8b* mutants were incubated in the same tube containing PBST solution with 1:200 Rhodamine Red conjugated anti-HRP (Jackson ImmunoResearch) and 1:200 RFP-booster (Chromotek) at room temperature for 2 hours. After washing with PBST for 3 times, the fillets were mounted on glass slide with Vectorshield mounting medium (Vector Labs). Confocal images were recorded using a Nikon A1 Confocal Laser Microscope System (Nikon). For imaging NMJ, a 60x oil objective was used to focus on muscle 6/7 NMJ on A3 segment. Excitation, emission, and exposure settings were kept constant among control and mutant fillets. Z-series images were taken at 1 micron steps and projected to a 2-dimensional image to visualize the axonal terminals at the NMJ. Image-Pro Plus software (Media Cybernetics) was used to analyze the immunofluorescence intensities of the projected images.

Fluorescence recovery after photobleaching (FRAP):

The TopFluor-PS or TopFluor-PIP₂ labeling and FRAP protocols followed that in our previous study (9). BHK cells grown on fibronectin-coated glass-bottom dishes were flash-labeled with ~20µg of TF-PS or TF-PIP₂. Cell imaging and photobleaching were performed using a 60X TIRF/1.49NA Oil emersion lens mounted on a Nikon A1 confocal microscope. Fluorescence measurements and calculations were carried out exactly as described (9). Normalized fluorescence intensity was averaged and used to plot the complete recovery curves shown as mean ± SEM. Independent measurements of mobile fractions and diffusion coefficients were pooled and shown as mean ± SEM. Statistical significance was evaluated in Student's *t*-tests.

Cytosolic Ca²⁺ imaging:

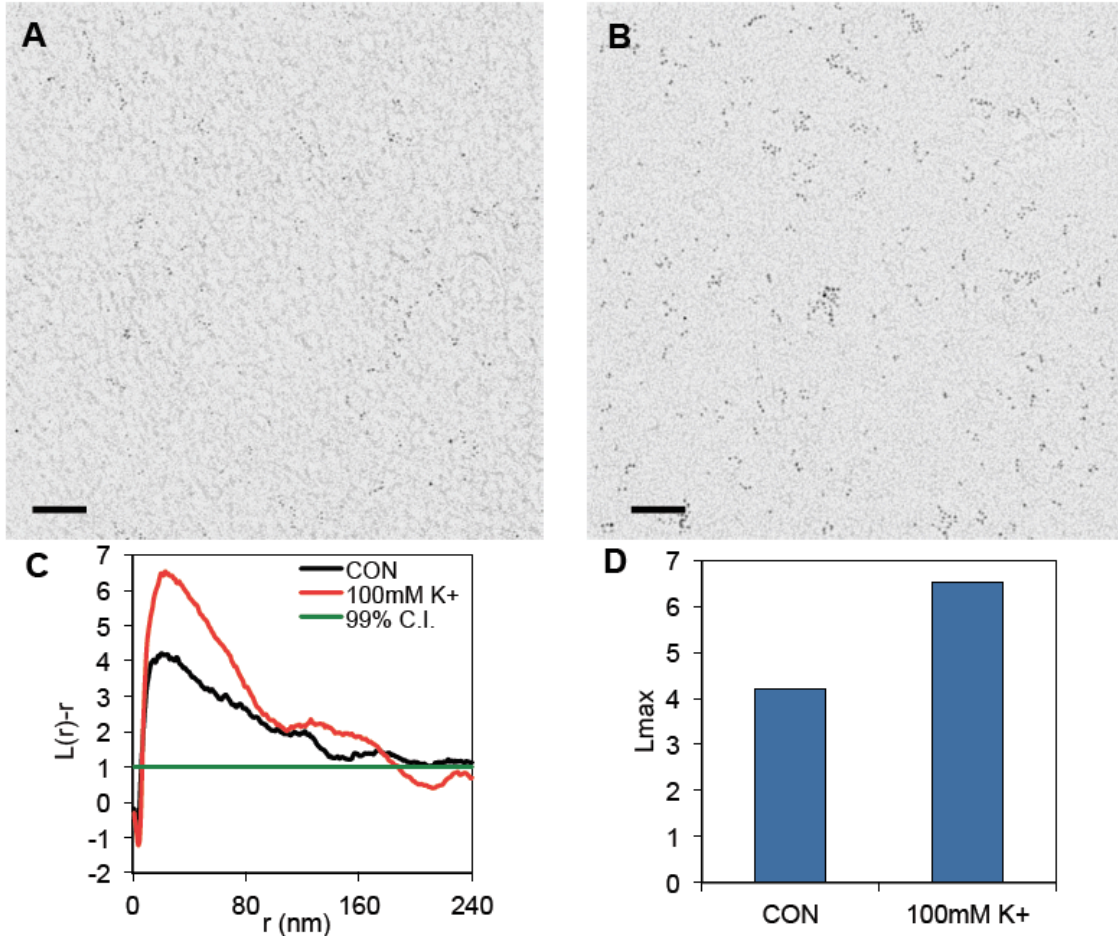
BHK or N2A cells seeded onto 15-mm coverslips and grown overnight to 70-80% confluency were washed with control HEPES buffer containing 5mM K⁺, pre-treated with 5 µM Fura-2AM/0.01% Pluronic acid (Molecular Probes) for 30 min at 37 °C and then washed with the same buffer. Ca²⁺ measurements were carried out at room temperature for the remainder of the experiment. Coverslips were mounted for viewing on a Nikon TE200 microscope. Imaging was performed with Incytm2 software (Intracellular Imaging, Inc.) at excitation wavelengths of 343/380 nm and emission wavelength of 520 nm. Baseline measurements were obtained for 2 min, followed by replacement of buffer by perfusion for two minutes. Measurements were taken for the specified time periods.

Annexin V labeling and flow cytometry:

BHK cells were seeded in 10-cm dishes and grown to ~70-80% confluency. Upon treatment, cells were detached from dish surface using DMEM/10% BCS containing 0.015% EDTA and washed with cold PBS. Annexin V labeling was performed according to the manufacturer's instructions (eBioscience Annexin V Apoptosis Detection Kit eFluor® 450). Flow cytometry was conducted immediately after Annexin V labeling

using BD LSRFortessa flow cytometer as described previously (13). Overnight incubation with 20 μ M camptothecin was used as positive control to induce PS externalization.

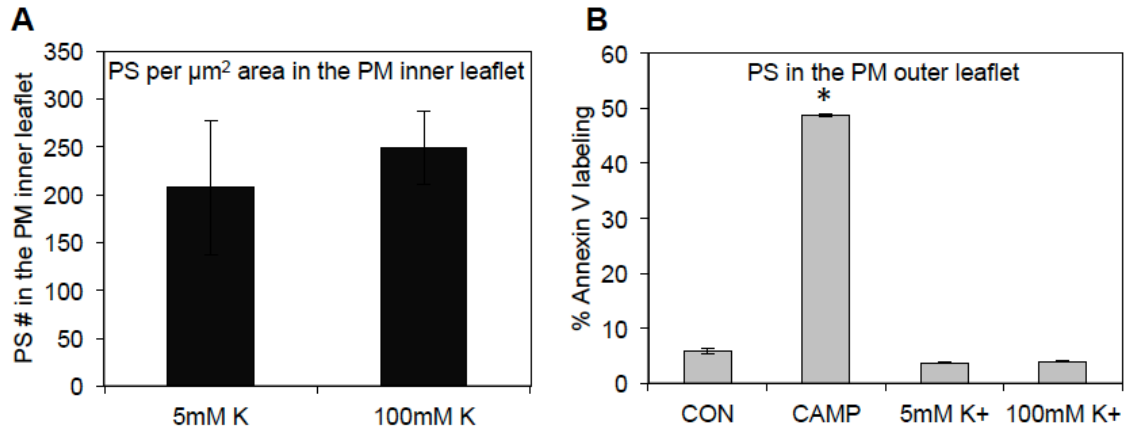
Fig. S1.



EM images of GFP-LactC2 nanoclustering in response to PM depolarization .

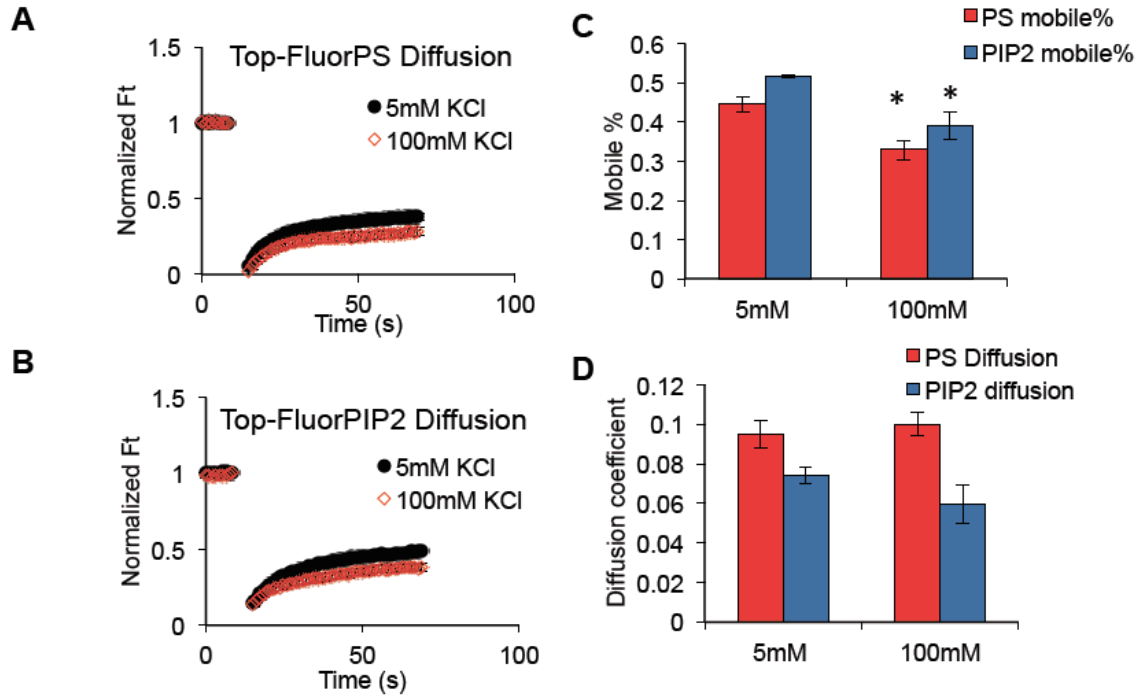
Sample EM images of 2D-plasma membrane sheets prepared from BHK cells expressing GFP-LactC2 (lactadherin C2 domain that specifically detects PS) and incubated in HEPES buffer containing 5mM K⁺ (A) or 100mM K⁺ (B), attached to EM grids, fixed with PFA /glutaraldehyde and labeled with 4.5nm gold coupled directly to anti-GFP antibody. Scale bar = 100nm in length. (C) The univariate K-functions ($L(r)-r$) of **a** and **b** are shown together with the summary statistic L_{max} for each pattern, where L_{max} = the maximum value of the $L(r) - r$ curve. (D). Similar EM-spatial mapping experiments were performed using lipid probes, such as GFP-Spo20 (PA-binding domain derived from *Saccharomyces cerevisiae* protein Spo20), GFP-PH-PLC δ (pleckstrin homology, PH, domain of phospholipase C-delta specifically for binding to PIP₂) and GFP-PH-Akt (PH domain of Akt and a PIP₃ probe). For all EM-spatial mapping experiments shown in this study, at least 15 images of PM sheets were obtained in each condition. Statistical analysis was conducted using bootstrap tests as constructed previously (4).

Fig. S2



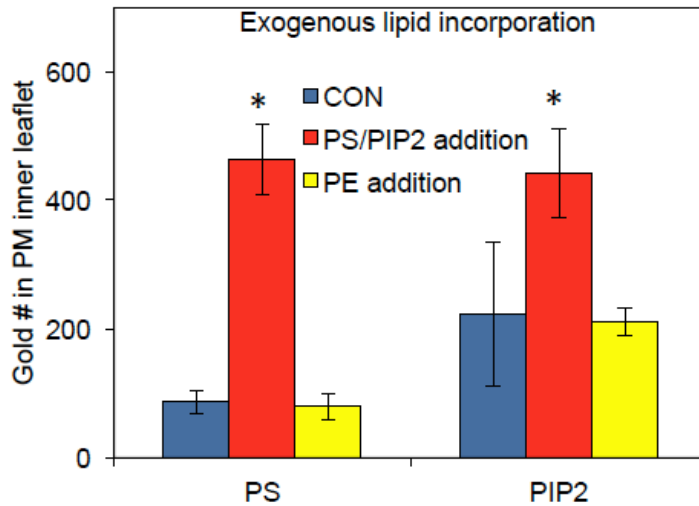
PM depolarization had no effect on PS localization in the PM inner leaflet. (A) BHK cells expressing GFP-LactC2 (specifically binds to PS in the PM inner leaflet) were incubated in HEPES buffer containing either 5mM or 100mM K⁺ for 60 minutes. Intact PM sheets of the BHK cells were attached to EM grids and labeled with 4.5nm gold nanoparticles coupled to anti-GFP antibody. The number of gold particles per μm^2 area on the PM inner leaflet directly reflects the amount of PS in the PM inner leaflet. (B) Amount of PS in the PM outer leaflet was measured using Annexin V labeling. Camptothecin (CAMP, 20 μM overnight) was used as positive control in the Annexin V labeling experiments. Camptothecin induces apoptosis, which leads to PS externalization and display of PS in the PM outer leaflet. Note that 100mM K⁺ did not change Annexin V labeling when compared to the untreated control, demonstrating that PM depolarization does not change the PS level in the PM outer leaflet and thus does not inhibit PM flippases.

Fig. S3



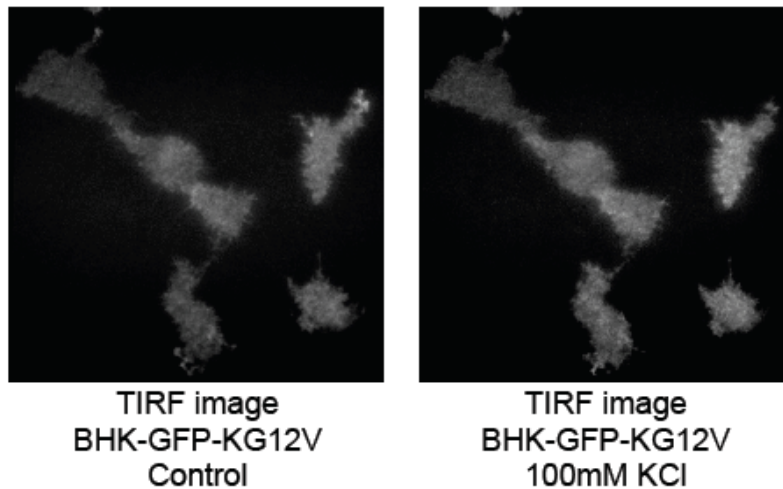
Immobile fraction of PS and PIP₂ increases on plasma membrane depolarization. Diffusion of TopFluor-PS or TopFluor-PIP₂ in BHK cell plasma membrane measured using FRAP. **(A)** Averaged normalized fluorescence recovery curves of TopFluor-PS in BHK cells suspended in either 5mM K⁺ (control HEPES buffer) or 100mM K⁺. **(B)** Averaged normalized fluorescence recovery curves of TopFluor-PIP₂ in BHK cells suspended in either 5mM K⁺ (control HEPES buffer) or 100mM K⁺. **(C)** Calculated mobile fraction of TopFluor-PS or TopFluor-PIP₂ is shown as mean \pm SEM from at least 15 cells. **(D)** Calculated diffusion coefficients of TopFluor-PS or TopFluor-PIP₂ are shown as mean \pm SEM from at least 15 cells. TopFluor-PS or TopFluor-PIP₂ report on inner leaflet dynamics because exogenous PS and PIP₂, whilst delivered to the outer PM leaflet, are rapidly displayed on the inner leaflet (Fig.S4).

Fig. S4.



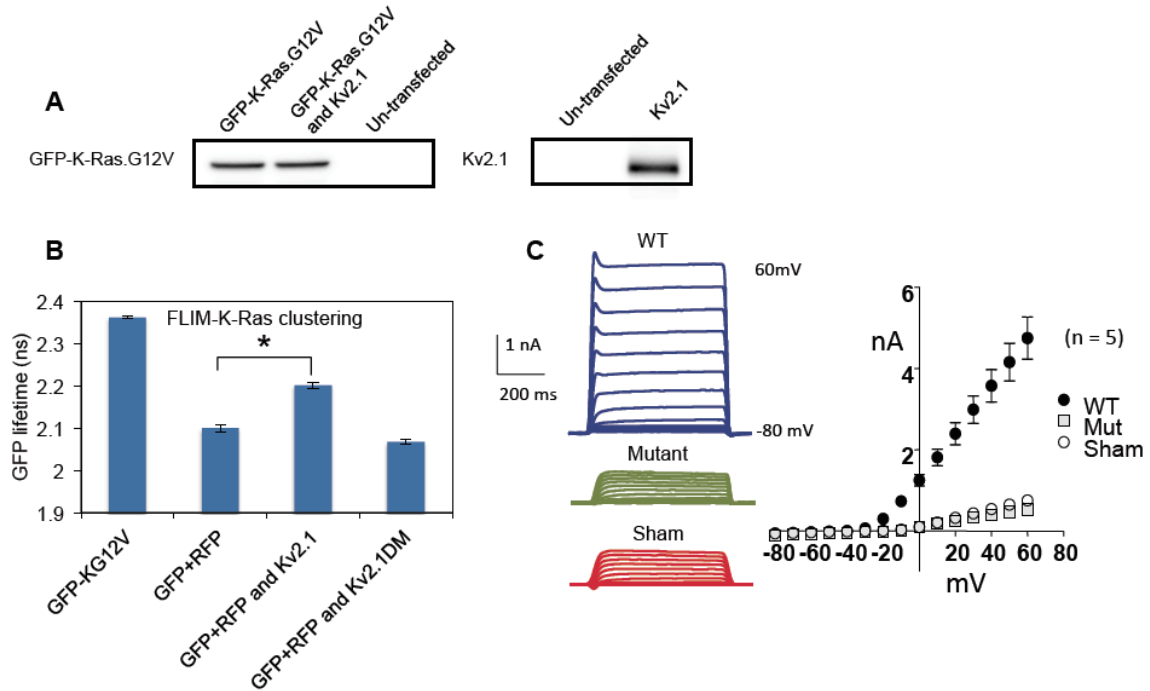
Exogenous PS and PIP₂ are efficiently incorporated into the inner leaflet of the plasma membrane. PSA-3 cells expressing either GFP-LactC2 (PS binding probe) or GFP-PH-PLC δ (PIP₂ binding probe) were grown in medium containing dialyzed FBS for 72 hours to deplete PS. PSA-3 cells were then incubated in the presence of various exogenous lipids, including brain PS, brain PIP₂ or brain phosphatidylethanolamine (PE), for 1 hour before harvesting. PM sheets attached to the EM grids were then labeled with 4.5nm gold nanoparticles and imaged using transmission EM. The number of gold particles per μm^2 area in the inner leaflet of the plasma membrane of PSA-3 cells reflects the amount of PS or PIP₂ in the PM inner leaflet. The result shows that exogenous PIP₂ indicate that exogenous PS and PIP₂ lipids are effectively incorporated into the inner leaflet of the plasma membrane. PE was a negative control included to validate the lipid-binding specificity of GFP-LactC2 or GFP-PH-PLC δ . The experiment also indicates that the exogenous lipids were not modified during the experiments as specific C2 and PH-binding domains selectively recognized significant increases in PS and PIP₂ in the PM inner leaflet.

Fig. S5.



Plasma membrane localization of GFP-K-RasG12V is insensitive to V_m . BHK cells stably expressing GFP-K-RasG12V were grown in a 3.5cm glass-bottom dish overnight and placed in a perfusion chamber on the stage of a total internal reflection fluorescence (TIRF) microscope. HEPES buffers containing control 5mM K^+ or 100mM K^+ were flowed into the chamber and changes in GFP fluorescence intensity was monitored in real time. The image on the right was taken after 60min exposure to 100mM K^+ . The experiment shows that no GFP-K-RasG12V was lost from the PM as a result of extended PM depolarization. Additional confocal and FLIM imaging confirmed that there was no change in cell shape or volume during extended incubation of cells in isotonic 100mM K^+ .

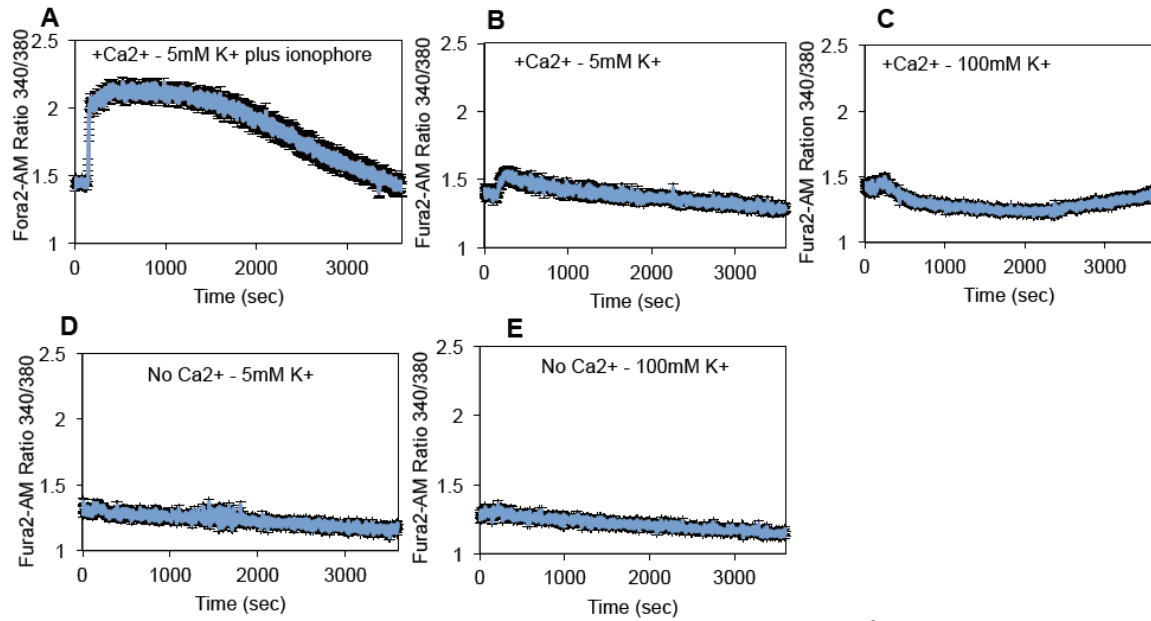
Fig. S6.



Plasma membrane hyperpolarization disrupts GFP-K-RasG12V nanoclustering.

BHK cells were transfected with GFP-K-RasG12V alone or with Kv2.1. (A) Co-expressing Kv2.1 had no effect on the level of expression of GFP-K-RasG12V in BHK cells. Expression of Kv2.1 was validated using a Kv2.1-specific antibody. (B) BHK cells expressing GFP-K-RasG12V alone (GFP-KG12V) or a combination of GFP-K-RasG12V and RFP-K-RasG12V (G/R-KG12V) with or without Kv2.1 were imaged using FLIM. Co-expressing the channel inactive double mutant Kv2.1W369CY384T (Kv2.1DM) did not change the fluorescence lifetime of GFP-K-RasG12V. Each data point is the mean (\pm SEM) GFP lifetime measured in >60 individual cells. Significant differences (* p <0.001) were evaluated using one-way ANOVA. (C) Channel activity of wild-type Kv2.1 (WT) and Kv2.1 channel non-conducting double mutant (Mut) was evaluated using patch clamping.

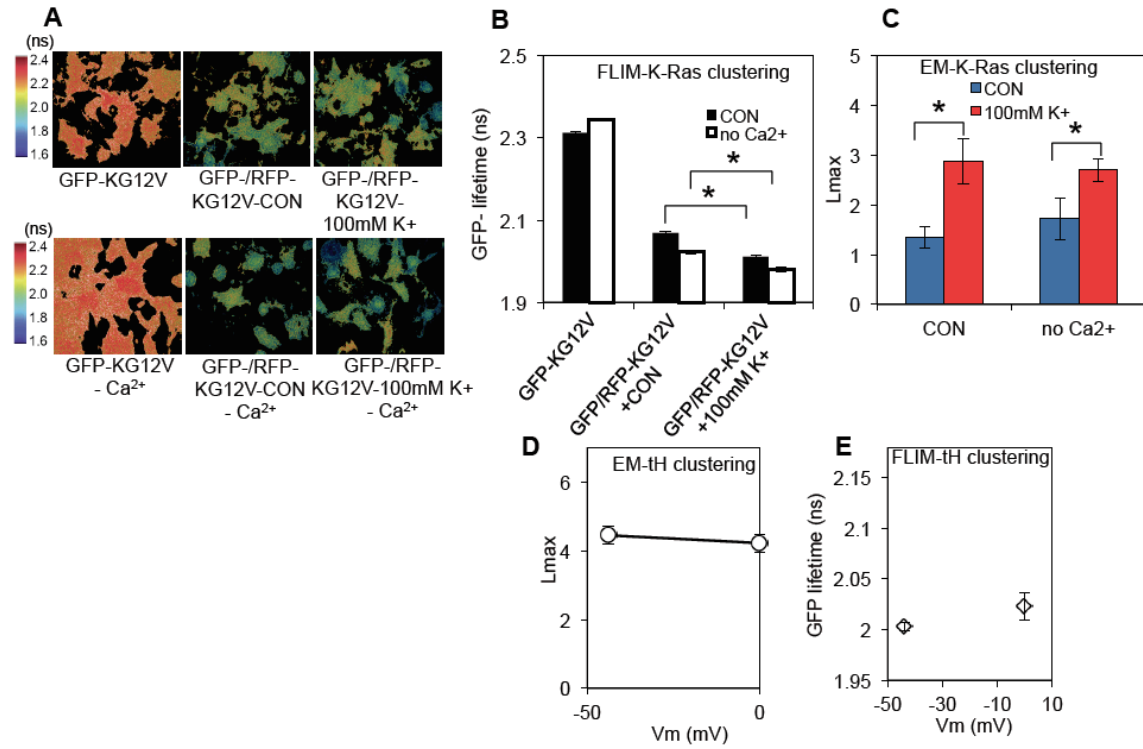
Fig. S7.



Plasma membrane depolarization has no effects on cytosolic Ca^{2+} level. (A)

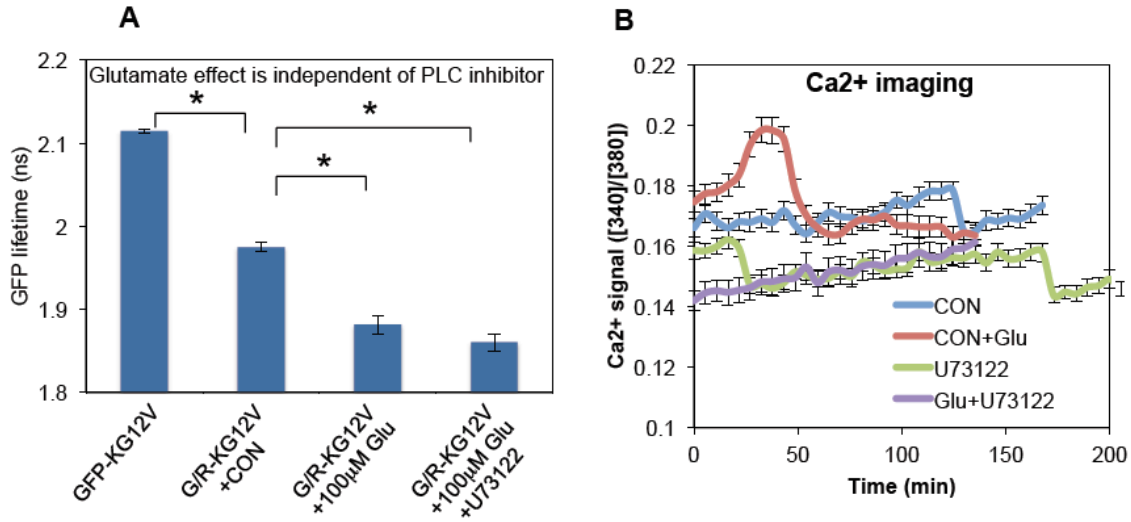
Fluorescence of Fura-2 incorporated in the cytosol of BHK cells was monitored in HEPES buffer containing 5mM K^+ , 1mM Ca^{2+} and ionophore as a positive control. Cytosolic Ca^{2+} level was markedly elevated in the presence of ionophore and 1mM Ca^{2+} in the suspending buffer. (B) Fura-2 fluorescence was unchanged when BHK cells were switched to HEPES buffer containing 5mM K^+ and 1mM Ca^{2+} in a perfusion chamber. (C) Fura-2 fluorescence was unchanged in BHK cells when perfused with HEPES buffer containing 100mM K^+ and 1mM Ca^{2+} . (D) No change in Fura-2 fluorescence was observed in BHK cells when buffer was switched to HEPES buffer containing 5mM K^+ with no Ca^{2+} and 1mM EGTA. (E) No change in Fura-2 fluorescence was observed in BHK cells when buffer was switched to HEPES buffer containing 100mM K^+ , no Ca^{2+} and 1mM EGTA. This experiment shows that changing external $[\text{K}^+]$ had no effect on cytosolic Ca^{2+} levels.

Fig. S8.



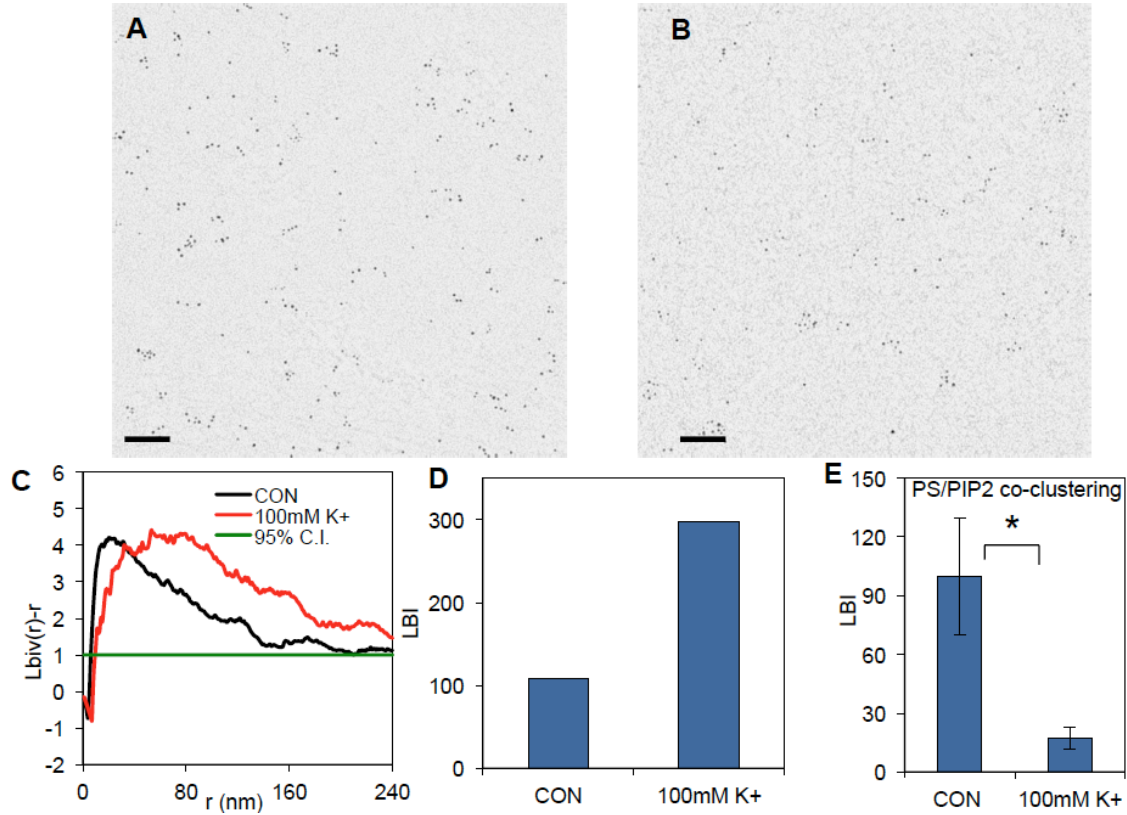
Plasma membrane depolarization-induced changes in GFP-K-RasG12V nanoclustering are independent of Ca²⁺ flux. BHK cells expressing GFP-K-RasG12V alone (GFP-KG12V) or coexpressing GFP-K-RasG12V and RFP-K-RasG12V (GFP-/RFP-KG12V) were incubated in HEPES buffers containing 5mM [K⁺] (CON) or 100mM [K⁺] with either 2mM Ca²⁺ in the buffer or with no Ca²⁺ plus 1mM EGTA. Representative FLIM images are shown in (A) and the experiment quantified in (B). Each data point is the mean (\pm SEM) GFP lifetime measured in >60 individual cells. Significant differences (* p <0.001) were evaluated using one-way ANOVA. (C) GFP-K-RasG12V nanoclustering on PM sheets prepared from BHK cells treated as in A and B was analyzed using univariate K-functions (shown as L_{max} values). PM depolarization induces the same extent of enhanced K-Ras clustering irrespective of the presence or absence of Ca²⁺. Significant differences were evaluated in bootstrap tests (* p =0.001). (D) Extent of nanoclustering as shown in L_{max} values of GFP-tH at 5 or 100mM K⁺, obtained via EM-spatial mapping technique. (E) Fluorescence lifetime of GFP-tH in cells expressing the cognate RFP-FRET pair plotted against V_m . Each data point is the mean (\pm SEM) GFP lifetime measured in >60 individual cells. Significant differences (* p <0.001) were evaluated using one-way ANOVA.

Fig. S9.



PLC inhibitor U73122 had no effect on the ability of glutamate to enhance GFP-K-RasG12V nanoclustering in N2A cells. (A) N2A cells expressing GFP-K-RasG12V alone (GFP-KG12V) or coexpressing GFP-K-RasG12V and RFP-K-RasG12V (G/R-KG12V) were incubated in DMEM medium without/with 100μM glutamate with/without 10 minute pre-treatment of 10μM U73122. Each data point is the mean (\pm SEM) GFP lifetime measured in >60 individual cells. Significant differences (* p <0.001) were evaluated using one-way ANOVA. (B) Addition of PLC inhibitor effectively inhibited Glutamate-induced elevation of Ca²⁺ level in the cytosol.

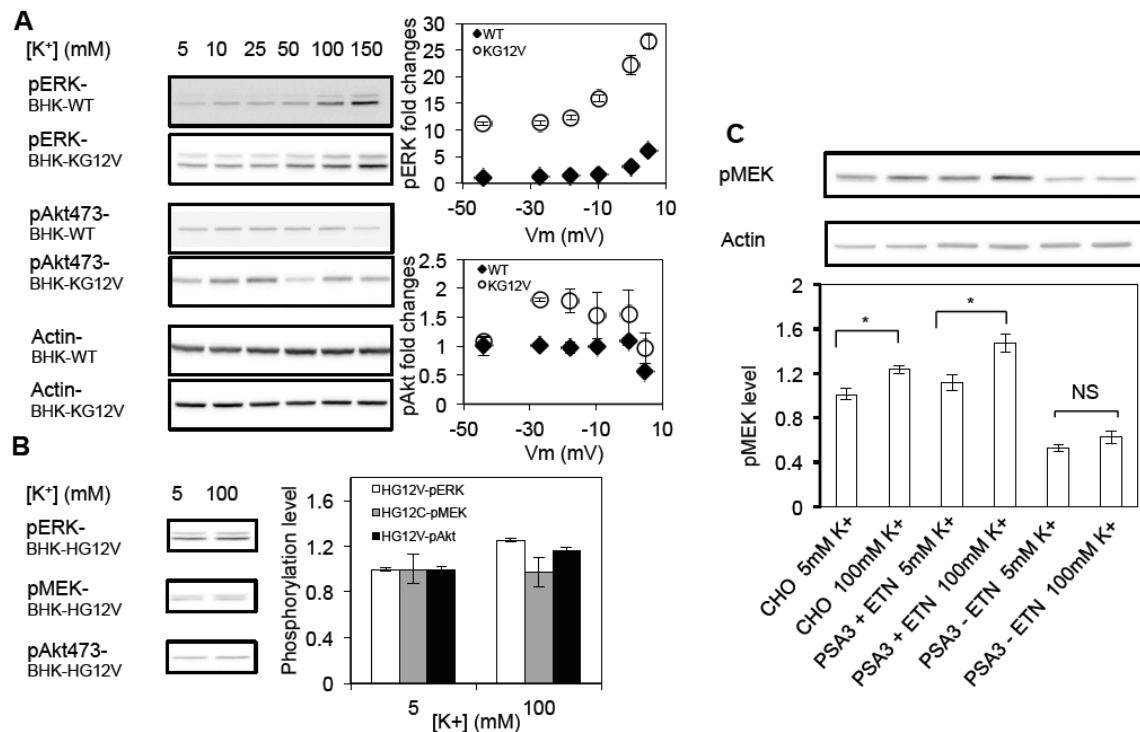
Fig. S10.



PM depolarization enhances co-clustering between PS and K-RasG12V. Sample EM images of 2D-plasma membrane sheets prepared from BHK cells co-expressing GFP-LactC2 and RFP-K-RasG12V and incubated in HEPES buffer containing 5mM K⁺ (A) or 100mM K⁺ (B) attached to EM grids, fixed with PFA / glutaraldehyde, and labeled with 6nm gold coupled to anti-GFP antibody and 2nm gold linked to anti-RFP antibody. Scale bar = 100nm. (C) The bivariate K-functions ($L_{biv}(r)-r$) from A and B are shown, together with the summary statistic LBI for each pattern (D).

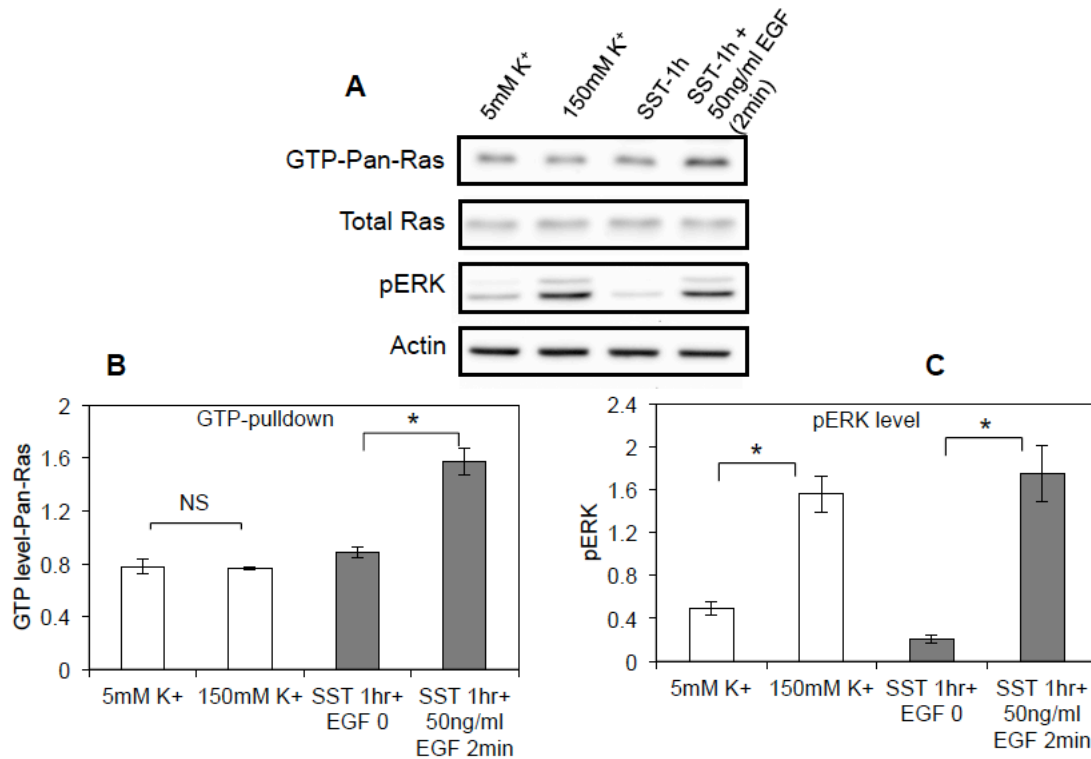
(E) Bivariate co-clustering between GFP-LactC2 and RFP-PH-PLC δ quantified as LBI values in cells incubated in 5mM K⁺ (CON) or 100mM K⁺. These bivariate EM experiments show that PM depolarization caused a decrease in LBI values, indicating increased segregation of PS away from PIP₂ upon PM depolarization. This is consistent with Fig.3A, which shows that PS was depleted from GFP-tH clusters on PM depolarization. GFP-tH clusters overlap with lipid raft-like domains, which are enriched in PIP₂.

Fig. S11.



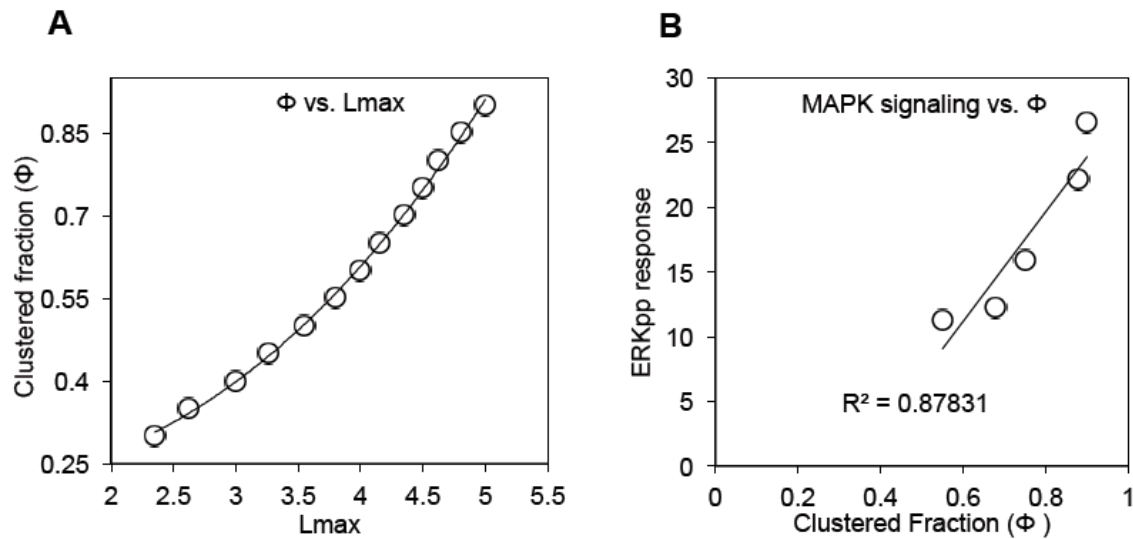
PS mediates PM depolarization-induced increased K-Ras dependent MAPK signaling. (A) Western blots of pERK and pAkt in wild-type BHK cells (BHK-WT) and BHK cells stably expressing K-RasG12V (BHK-KG12V) incubated in increasing [K⁺]. Quantitation of 3 independent experiments is also shown as mean \pm SEM. The magnitude of V_m -induced changes in pERK levels was smaller in wild type BHK cells. This appeared not to result from Ras activation because there was no change in abundance of Ras.GTP in wild type cells after membrane depolarization (Fig.S12). Thus, MAPK activation in wild-type cells is likely mediated by enhanced nanoclustering of basal GTP-bound K-Ras. PM depolarization had no effect on the phosphorylation of Akt (A) in K-RasG12V cells. Most likely because K-Ras is a more potent activator of the Raf-MEK-ERK cascade than it is of PI3K-Akt (3). (B) Blots and quantitation of pMEK, pERK and pAkt in BHK cells stably expressing H-RasG12V incubated in 5mM or 100mM K⁺. (C) MAPK signaling was evaluated in parental CHO cells expressing GFP-K-RasG12V or PSA3 cells expressing GFP-K-RasG12V. PSA3 cells were grown in media with or without ethanolamine. Cells were then briefly incubated in HEPES buffer containing 5mM or 100mM K⁺. Whole cell lysates were collected and blotted for phosphorylated MEK.

Fig. S12.



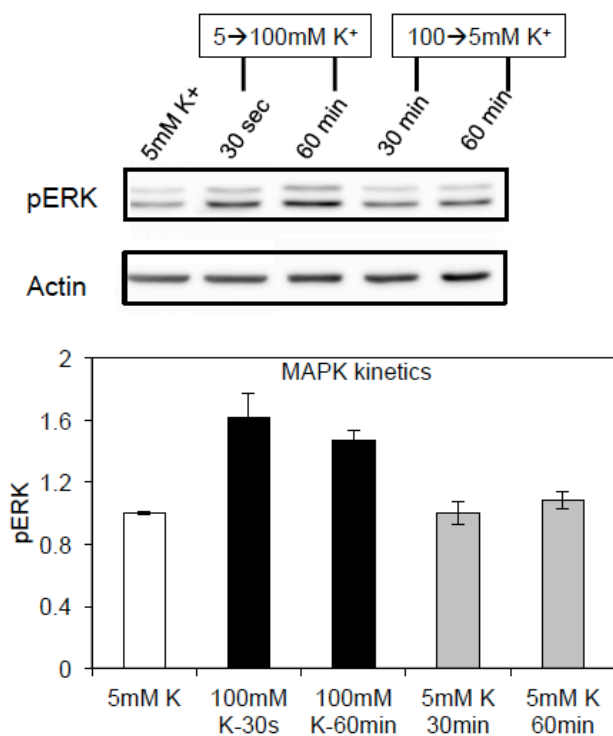
PM depolarization increased MAPK signaling without affecting level of GTP-bound K-Ras in wild type BHK cells. (A and B) Level of GTP-bound Ras was measured using a Ras-GTP-pull-down assay (5). Wild-type BHK cells were incubated in HEPES buffer containing either 5mM K⁺ or 150mM K⁺ for 1 hr before harvesting. For a positive control, wild-type BHK cells were serum-starved (SST) for 1 hr and stimulated with 50ng/ml EGF for 2 minutes. (C) MAPK signaling upon PM depolarization or EGF stimulation was evaluated in wild-type BHK cells.

Fig. S13.



MAPK signal output is dependent on the clustered fraction. (A) K-Ras clustered fraction (Φ) is non-linearly correlated with the extent of nanoclustering (Lmax). Clustered fraction values were extracted from Monte Carlo simulations of the established clustering model described in Plowman et al. (Ref 4). (B) MAPK signal output from Fig.3D was plotted against clustered fraction (Φ).

Fig. S14.



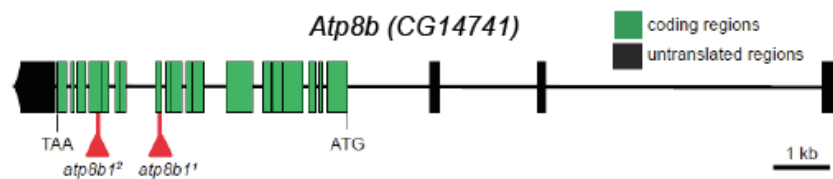
MAPK signaling responds to PM depolarization rapidly and reversibly. Levels of phosphorylated ERK during PM depolarization and re-polarization were measured using Western blotting.

Fig. S15.

A

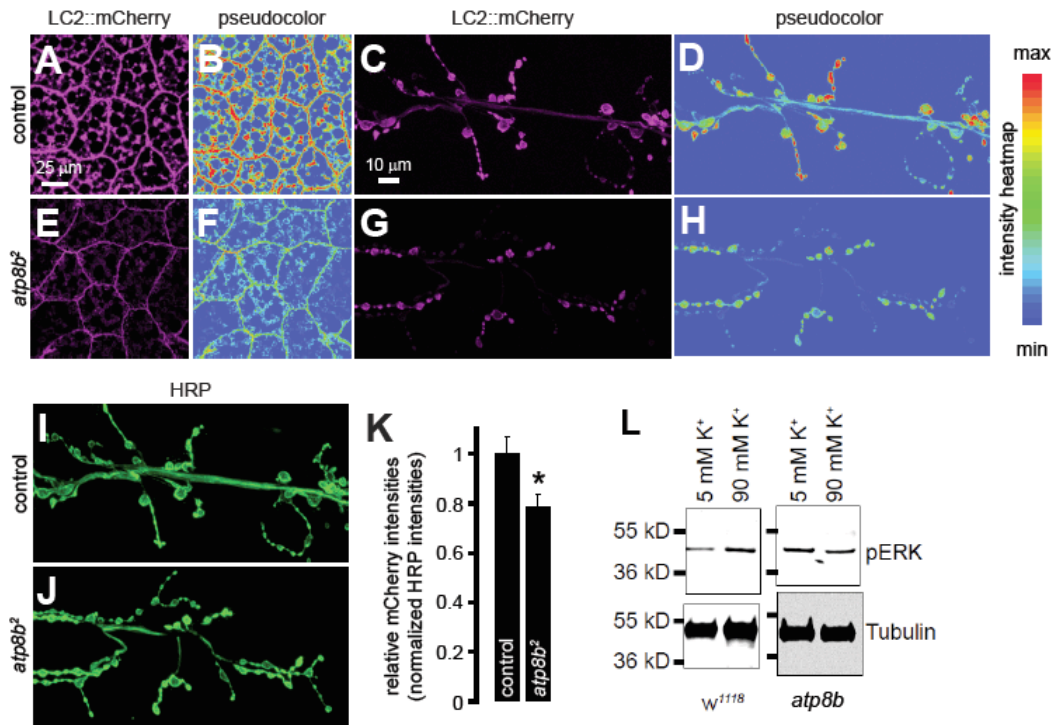


B



Alignment of vertebrate and fly *atp8b* (A) and the genomic locus of *atp8b* (B).

Fig. S16.



Levels of PS in the inner leaflet of the plasma membrane are diminished in the *atp8b*² larvae. (A and E) Representative confocal images of 3rd larval fat bodies of the genotypes indicated on the left expressing the PS sensor, LC2-mCherry. (B and F) Heatmaps showing the range of mCherry fluorescence intensities in (A) and (E) respectively. (C and G) Representative confocal images of 3rd larval neuromuscular junction (NMJ) synapses of the indicated genotypes expressing LC2-mCherry. (D and H) Heatmaps showing the range of mCherry fluorescence intensities in (C) and (G) respectively. Colors corresponding to the maximum and minimum fluorescent intensities in the heatmaps are shown in the bar on the right. (I and J) Representative confocal images of 3rd larval NMJ synapses of the indicated genotypes stained with antibodies against Horse Radish Peroxidase (HRP) to visualize the presynaptic axons. (K) Bar-graph showing the relative mCherry fluorescent intensities normalized to the HRP fluorescent intensities at the NMJs from larvae of the indicated genotypes. (L) Fly embryos from wild-type flies and mutant *atp8b* flies were incubated in buffers containing either 5mM [K⁺] or 90mM [K⁺] for 15 minutes and then harvested and immunoblotted for pERK (or tubulin = loading control).